Multi-technique analysis of an ancient stratified glass eye bead by OCT, μ-XRF, and μ-Raman spectroscopy

Junqing Dong (董俊卿)[1,2], Qinghui Li (李青会)[1,2,*], and Yongqing Hu (胡永庆)[3]

[1]*Sci-Tech Archaeology Center, Laboratory of Micro-Nano Optoelectronic Materials and Devices, Key Laboratory of Materials for High-Power Laser, Shanghai Institute of Optics and Fine Mechanics, Chinese Academy of Sciences, Shanghai 201800, China*

[2]*Center of Materials Science and Optoelectronics Engineering, University of Chinese Academy of Sciences, Beijing 100049, China*

[3]*Henan Provincial Institute of Cultural Relics and Archaeology, Zhengzhou 450000, China*

**Corresponding author: qinghuil@sina.com*

Received February 8, 2020; accepted May 15, 2020; posted online July 20, 2020

In this Letter, we report a combination of non-invasive analysis of the cross-section structure, phase, and chemical composition combining optical coherence tomography (OCT) with spectroscopic methods such as X-ray analytical microscope (μ-XRF) and micro-Raman spectroscopy (μ-RS), which allow us to effectively and conveniently identify the colorants used for each color region and the glass-making process of an ancient multicolored stratified glass eye bead. The results reveal that the sophisticated colors of the glass bead arise from the transition metals and chemical compound crystals deliberately added in the same base glass and carefully adjusted by the glass maker to obtain four colors. We also propose and discuss the provenance of the glass bead. It was probably introduced to China through the Northern Silk Road from Egypt or the Eastern Mediterranean areas about 1400 years ago. The combined multi-analytical technique is the promising approach for precious cultural heritage research.

Keywords: multi-spectroscopic methods; combination of non-invasive analysis; ancient stratified glass; cross-section structure; chemical composition; glass-making process.

doi: 10.3788/COL202018.090001.

Some of the optical and spectroscopic techniques that were initially developed for the fields of chemistry, biology, biomedicine, materials sciences, and geology are used as important methods to characterize the micro-structure, elemental composition, coloring and opacifying agents, and secondary phases of archaeological materials. The common techniques are optical microscopy, optical coherence tomography (OCT)[1,2], synchrotron radiation micro-computed tomography (SR-μCT)[3], laser ablation inductively coupled plasma atomic emission spectrometry or mass spectrometry (LA-ICP-AES/MS)[4], scanning electron microscopy coupled with an X-ray energy dispersive spectrometer (SEM-EDS)[5], proton induced X-ray emission (PIXE)[6], micro-Raman spectroscopy (μ-RS)[7], X-ray fluorescence spectrometry (XRF)[8], X-ray analytical microscopy (μ-XRF)[9], and so on. Constrained by the effects of the shape or uneven surface of samples and limitations of the instrument itself, the information obtained by a single technique is insufficient, while the combination of multiple techniques is beneficial to realizing mutual complementation and verification. In recent years, these analytical instruments have been increasingly widely applied in research on biomedicine[1,9–11] and cultural heritage (i.e., ceramic[2,12], porcelain[13,14], potsherd[15,16], glass[3,8], polychrome sculpture[17], and amalgam mirror[18]).

As a non-contact method, OCT technology can quickly and conveniently generate high-resolution cross-sectional and three-dimensional images of the subsurface of transparent and translucent materials. μ-XRF is a non-destructive technique for simultaneous qualitative and quantitative analyses of chemical components of points, lines, and areas. μ-RS can obtain information on both microscopic morphology and the phase at the same time; especially, for ancient material, it can also identify pigments and opacifiers, as well as provide further information on the type of glassy matrix. For instance, Colomban and coworkers have analyzed great quantities of archaeological glasses and glazed ceramics by means of Raman spectroscopy (RS)[7,19–21].

The eye bead (Fig. 1), as a popular ornament in ancient time, first appeared in the 18th Dynasty of ancient Egypt (1550 B.C.–1307 B.C.)[22] and was soon prevalent in North Africa, Western Asia, and Southern Europe. Eye beads originated from the eye of ancient Egyptian god statues, most of which were inlaid with glass or gemstones in the shape of eyes. The eye bead was considered a protection against evil spirits by ancient Egyptians. Western Asians thought that the god eyes with incomparable power can drive away ghosts and evil spirits and bring safety[23]. During the Spring and Autumn Period and Warring States Period (about mid-eighth century B.C. to mid-fifth century B.C.), glass eye beads were introduced gradually to the Xinjiang, Inner Mongolia, Gansu, Shaanxi, Shanxi, Henan, Hubei, Hunan, Chongqing, and Anhui Provinces through the Silk Road[24–27] and were considered to be significant evidences of cultural and economic exchanges

Fig. 1. Eye beads unearthed from Chu tomb in Xujialing, Xichuan, Henan Province.

between China and the West. The map marking the Silk Road and these localities can be found in the literature[24,25]. The eye bead is a kind of elegant ancient craft with exquisite workmanship, usually made of a colored matrix, eye circles, and eye balls.

In previous studies, some scholars have analyzed eye beads unearthed in Xujialing and Shenmingpu, Henan Province, Leigudun, Wangshan, and Jiudian, Hubei Province, and Lijiaba, Hunan Province using PIXE[6], XRF[28], LA-ICP-AES[4], X-ray diffractometry (XRD), SEM-EDS[5], μ-RS[8], SR-μCT[3], and OCT[29] and discussed the chemical composition system and colorant. However, it is sometimes difficult to apply all of the above-mentioned techniques on glass beads for their size, shape, and limited possibilities of sampling because modern ethics of archaeology prohibit destructive analyses generally. The researcher wishing to use one or more of the analytical techniques should consider the merits and drawbacks of each technique and determine which is the best for what information is desired[30]. For example, as a useful technique for both observation and elemental analysis, SEM-EDS requires sections with a polished surface and coating for semi-quantitative analyses. In general, the researcher has to make an appointment for SR-μCT analysis at least half a year in advance. Limitation of the size of the beam diameter (1–3 mm) of the routine XRF and PIXE makes it unable to accurately observe the existent elements in the extremely thin area for the globular and irregular samples without preparation. It is difficult to obtain ideal phase information on the micro-sized crystalline particles from the untreated surface of glass artifacts employing the routine XRD method. It is, therefore, necessary to explore a new convenient combined approach with no sampling or sample preparation for cross-sectional structure and micro-phase analyses and quantitative determination of precious cultural relics to characterize their making techniques, homogeneity, and recipes.

In this Letter, we report a combined investigation on the material, chemical composition, phase, fluxing agent, colorant, cross-sectional structure, craftsmanship, and provenance of an ancient eye bead using non-destructive swept source OCT (HSL-2100, Santec, Japan)[2], μ-XRF (XGT 9000, Horiba Ltd., Japan), and μ-RS (LabRAM XploRA, Horiba Jobin Yvon, France)[5,31] techniques, supplemented with digital microscopy (VHX-5000, KEYENCE Company, Osaka, Japan). Eleven integral eye beads (Fig. 1) and a broken bead [Fig. 2(a)] were unearthed from tomb No. 10, one nobleman of the Chu State dated to the Early Warring States Period (~475 B.C.–350 B.C.) in Xujialing, Xichuan, Henan Province. These beads have similar shapes, with two nearly plane ends and a central hole, sky blue body, dark blue pupil, and ochre circle pattern on the inlaid white eye ball. The bodies of two of them are nearly column and nine are globular. The sizes are 1.15–1.90 cm height, 1.40–2.10 cm max diameter, and 0.16−0.52 cm aperture.

Firstly, we obtain the 3D pseudo-color images of the eye bead and the slice images at different angles using OCT (Fig. 2). The OCT system employed herein (HSL-2100, Santec) consisted of a swept light source with a central wavelength of 1315−1340 nm, and a high scan speed of 20 kHz. As such, a 5.3 μm longitudinal spatial resolution in silicate materials with a 1.5 refractive index was estimated, along with a 12 μm lateral spatial resolution in air. The imaging range was 0−20 mm. The eye bead presents obviously different uniformity and transmissivity among turquoise blue, dark blue, brown, and white color regions due to the different capacities of scattering and absorption of light. The dark blue eye ball with high transparency has strong capacity of light absorption, but a small number of scattering particles also were observed [Fig. 2(b)]. As shown in Figs. 2(c), 2(d), and 2(e), the dark blue eye ball did not traverse the entire bead, but was inlaid into the white eye circle and turquoise blue matrix; the opaque white eye circles are dominated by uniform scattering phase; numerous scattering particles are

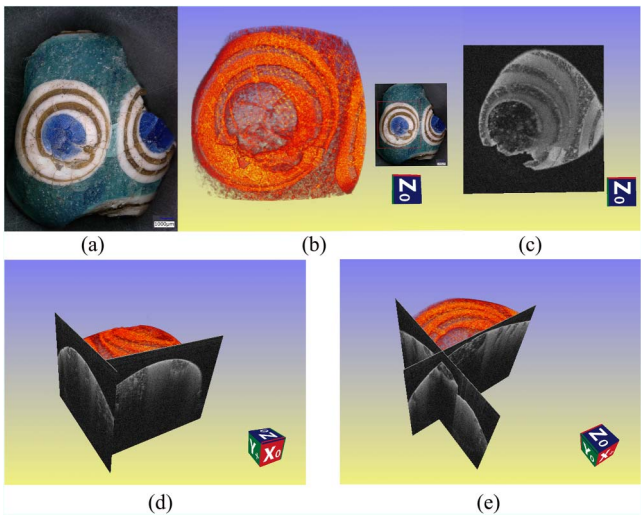

Fig. 2. Micrograph and 3D pseudo-color OCT images of the eye bead HXX-M10. (a) Micrograph of the broken bead; (b) top view and the position; (c) slice perpendicular to the z axis, positioned at a distance of 184 pixels from the top; (d), (e) 3D sliced diagrammatic sketch at different angles along the x and y axes.

distributed in the low-transparency turquoise blue matrix, while the brown circles fall in between the dark blue eye ball and turquoise blue matrix in terms of light absorption property and transparency.

The bead was scanned in detail by OCT to obtain more structure characteristics of different color regions. Figure 3 shows the 2D images of optical scattering from internal micro-structures. Different color regions have distinct boundaries due to the diverse light-scattering and absorption properties [Figs. 3(a)–3(d)]. Scattering particles distributed in the turquoise blue matrix and brown layers are probably related to the crystallization during the glass-melting operation. Comparatively speaking, many more and larger scattering particles are observed in the turquoise blue matrix than in the brown layers. Several different sizes of bubbles can be found in the dark blue eye ball [Figs. 3(d) and 3(e)]. The large bubbles appeared to be elliptical with the white edges and black interior, while for the small bubbles, the edges present two nearly parallel lines. Many small bubbles are also observed in the brown layers [Fig. 3(d)], but there are basically no obvious bubbles in the turquoise blue matrix [Fig. 3(f)].

From the two-dimensional (2D)-OCT images, it can be seen that the white and brown layers are uneven in thickness, and the cross sections of the dark blue eye ball, white layers, and brown layers shrink gradually from the surface to the bottom. The decreasing tendency and the different transparencies of the four color regions also could be observed by optical microscopy (Fig. 4). According to the above analyses, we can infer that the stratified eye bead was produced by hot-working technology with the glass-making process as follows. Firstly, the turquoise blue matrix was produced, and then in a semi-solidified state, the white layer, brown layer, and dark blue eye ball were successively embedded in the matrix. As a result, the latter

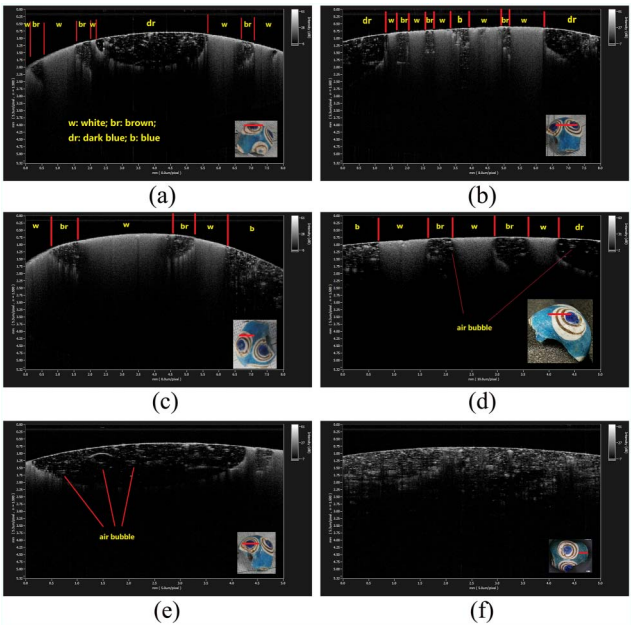

Fig. 3. 2D-OCT images of eye bead HXX-M10.

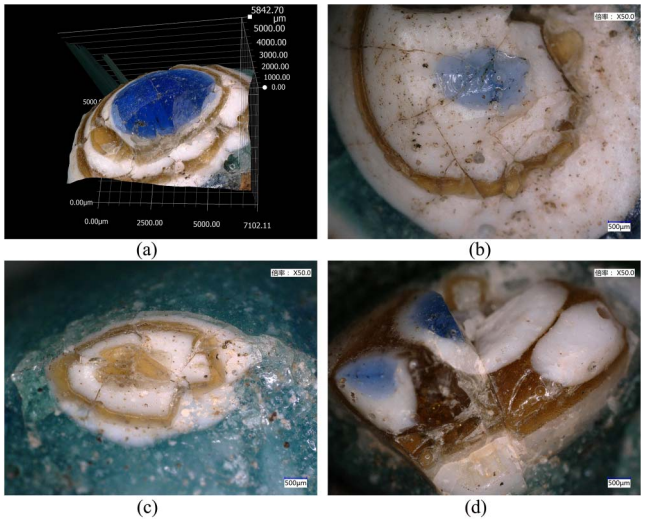

Fig. 4. Microscopic images of the fragments of eye bead HXX-M10.

colorized glass rod would squeeze and penetrate into the former ones, which is the probable reason why the white and brown layers appear uneven in thickness with varied boundaries [Figs. 4(a)–4(c)], and the color of the dark blue eye ball gradually fades from outside to inside along with the trend of reducing the diameter by degrees [Figs. 4(a) and 4(d)].

In order to ascertain the chemical composition of four color regions in the eye bead, a μ-XRF was used for elemental mapping and quantitative analysis under vacuum to improve the detection sensitivity of light elements. It was

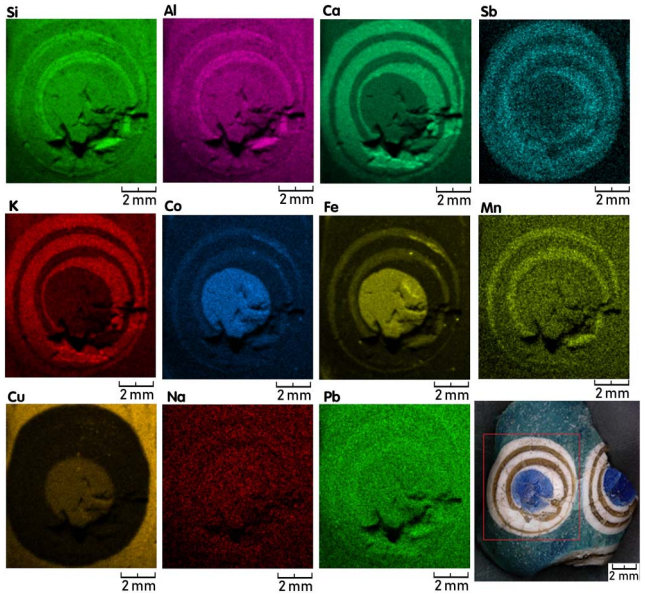

Fig. 5. Element mapping for eye bead HXX-M10 shows that the dark blue area has a correlation with elements of Co and Fe, the white area with Sb and Ca, the brown area with Fe and Mn, and the blue matrix with Cu. The lighter shade corresponds to higher concentrations.

Table 1. Chemical Composition of the Eye Glass Bead HXX-M10 Unearthed from Chu Tomb in Xujialing by μ-XRF[a] (wt%)

Color		Na_2O	MgO	Al_2O_3	SiO_2	Cl	K_2O	CaO	TiO_2	Fe_2O_3	CoO	CuO	Sb_2O_3	Mn_2O_3	ZnO	SnO_2	PbO	SO_3	SrO	BaO	ZrO_2
Mapping area		9.78	0.63	4.14	70.56	0.45	0.84	9.29	n.d.	0.79	0.01	0.28	2.67	0.03	n.d.	n.d.	n.d.	0.46	0.03	0.03	n.d.
Dark blue	1	7.79	0.58	n.d.	76.30	0.49	1.01	8.32	0.09	2.23	0.11	0.35	2.44	n.d	0.07	0.05	0.01	0.11	0.04	n.d.	n.d.
	2	15.81	0.35	n.d.	70.48	n.d.	0.77	7.44	0.07	1.94	0.10	0.28	2.29	n.d	0.06	0.09	0.01	0.27	0.03	n.d.	n.d.
	3	2.37	1.02	1.36	78.33	n.d.	1.24	9.73	0.12	2.51	0.13	0.42	1.94	n.d.	0.08	0.09	0.01	0.50	0.05	0.12	n.d.
	4	6.26	0.48	n.d.	77.01	0.68	0.07	9.06	0.11	2.48	0.13	0.40	2.47	n.d.	0.08	0.12	0.01	0.42	0.06	0.16	n.d.
	5	12.74	0.38	n.d.	73.27	n.d.	0.85	8.00	0.08	1.98	0.10	0.32	1.54	n.d.	0.06	0.10	0.01	0.37	0.04	0.17	n.d.
	Average	8.99	0.56	0.27	75.08	0.23	0.79	8.51	0.09	2.23	0.11	0.35	2.14		0.07	0.09	0.01	0.33	0.04	0.09	
	STD	4.76	0.24	0.54	2.84	0.29	0.39	0.80	0.02	0.24	0.01	0.05	0.35		0.01	0.02	0.00	0.13	0.01	0.08	
Turquoise blue	1	8.75	n.d.	0.44	78.72	0.46	1.65	7.39	0.06	0.37	n.d.	1.04	0.35	n.d.	n.d.	0.19	0.06	0.41	0.04	0.08	n.d.
	2	20.07	n.d.	0.35	70.78	0.37	1.14	5.75	0.04	0.27	n.d.	0.72	0.10	0.01	n.d.	0.11	0.04	0.12	0.03	0.10	n.d.
	3	0.34	n.d.	0.39	86.44	0.47	1.46	7.84	0.08	0.41	n.d.	1.20	0.42	n.d.	n.d.	0.31	0.06	0.41	0.04	0.11	n.d.
	Average	9.72		0.39	78.65	0.43	1.42	6.99	0.06	0.35		0.99	0.29	n.d.	n.d.	0.20	0.05	0.31	0.04	0.10	
	STD	8.08		0.04	6.39	0.04	0.21	0.90	0.02	0.06		0.20	0.14	0.00	n.d.	0.08	0.01	0.14	0.00	0.01	
Brown	1	22.11	n.d.	1.24	65.61	0.45	1.16	6.12	0.15	0.76	n.d.	0.01	1.82	0.06	0.01	0.05	0.01	0.41	0.03	n.d.	n.d.
	2	2.41	n.d.	0.92	82.28	0.68	0.98	8.07	0.12	0.94	n.d.	0.06	2.83	0.07	0.02	0.08	0.01	0.33	0.04	0.15	n.d.
	3	1.53	n.d.	0.99	82.56	0.70	1.01	7.81	0.13	0.93	n.d.	0.02	3.15	0.07	0.02	0.10	0.01	0.65	0.05	0.27	n.d.
	4	1.35	n.d.	0.43	82.89	0.73	0.92	8.26	0.14	0.97	n.d.	0.02	2.84	0.08	0.02	0.09	0.01	1.06	0.05	0.14	0.02
	Average	6.85		0.90	78.34	0.64	1.02	7.57	0.14	0.90		0.03	2.66	0.07	0.02	0.08	0.01	0.61	0.04	0.14	0.01
	STD	8.82		0.29	7.35	0.11	0.09	0.85	0.01	0.08		0.02	0.50	0.01	0.00	0.02	0.00	0.28	0.01	0.06	0.00
White	1	7.24	0.92	0.62	79.67	0.74	0.01	7.24	0.10	0.68	n.d.	0.01	2.09	0.05	n.d.	0.05	0.01	0.55	0.04	n.d.	n.d.
	2	0.49	n.d.	0.66	80.46	0.55	0.79	9.38	n.d.	0.54	n.d.	0.02	6.32	0.03	n.d.	0.09	0.02	0.61	0.05	n.d.	n.d.
	3	13.07	n.d.	0.69	75.46	n.d.	0.02	6.94	n.d.	0.46	n.d.	0.01	2.61	0.02	n.d.	0.10	0.02	0.55	0.04	n.d.	n.d.
	4	13.23	0.22	n.d.	71.58	n.d.	n.d	10.49	n.d.	0.37	n.d.	0.01	3.33	0.02	n.d.	0.06	0.03	0.44	0.04	0.19	n.d.
	5	0.12	n.d.	0.92	82.18	n.d.	0.06	8.13	n.d.	0.57	n.d.	0.04	6.81	0.03	n.d.	0.11	0.02	0.63	0.05	0.34	n.d.
	6	19.54	n.d.	0.28	68.26	n.d.	0.46	5.33	n.d.	0.28	n.d.	0.01	5.22	0.01	n.d.	0.03	0.01	0.38	0.03	0.14	n.d.
	7	0.13	n.d.	0.38	78.26	n.d.	0.62	8.32	n.d.	0.59	n.d.	0.04	10.46	0.02	n.d.	0.22	0.05	0.64	0.05	0.24	n.d.
	8	20.97	n.d.	0.79	64.94	0.39	0.47	7.36	n.d.	0.35	n.d.	0.01	3.94	0.02	n.d.	0.06	0.02	0.56	0.03	0.10	n.d.
	Average	9.35	0.14	0.54	75.10	0.21	0.30	7.90	0.01	0.48		0.02	5.10	0.03		0.09	0.02	0.55	0.04	0.13	
	STD	8.07	0.30	0.28	5.83	0.28	0.29	1.47	0.03	0.13		0.01	2.57	0.01		0.06	0.01	0.09	0.01	0.12	
Lower detection limit (ppm)		350	150	100	50	10	10	10	1	1	1	1	1	1	0.1	1	0.5	10	0.1	1	0.1

[a]"n.d." means not detected, i.e., the concentration of the oxide or element was below the instrumental detection limit; STD, standard deviation; lower detection limit is based on 7 mm spot size; lower detection limit varies depending on the sample matrix or coexisting elements; ppm, parts per million.

equipped with three types of optical illumination, coaxial (reflection), around (dark field), and transmission. Combining coaxial and around illuminations enables clear observation of samples with uneven or reflective areas. The spectrometer operates with a rhodium (Rh) X-ray tube and an energy dispersive, peltier cooled silicon drift detector, capable of detecting elements from sodium (Na) to uranium (U). The small X-ray spot size (down to 10 μm) and high spatial resolution allow for detailed analysis of the particles of tens of microns in size. In this Letter, analysis was carried out with the 100 μm X-ray beams. The mapping width and height are 8.448 mm (128 pixel) and 9.240 mm (128 pixel), respectively. Operational conditions were 50 kV tube high voltage, 0.5 mA tube current, and 20 s per point analysis time. Mapping analysis shows differences in chemical elements of the dark blue eye ball, turquoise blue matrix, brown layers, and white layers, which is closely related to cobalt and iron, copper, iron, and manganese, and calcium and antimony, respectively. Moreover, it seems that some antimony atoms are also present into the dark blue and brown regions (Fig. 5).

Quantitative chemical analyses reflect the typical composition of a natron-type soda-lime-silicate (Na_2O–CaO–SiO_2) glass (Table 1). In the mapping area, the main component is SiO_2, the glass network-forming oxide, with a mass fraction of 70.56 wt%, while the glass network-modifying alkali oxide Na_2O and the glass network-stabilizer alkali earth oxide CaO represent 9.78 wt% and 9.29 wt%, respectively. Other network modifiers, such as MgO (0.63 wt%) and K_2O (0.84 wt%), were found at low concentrations.

Considering the heterogeneity of the ancient glass artifact, several points of each color region were analyzed (the measurement positions are reported in the Supplementary Materials) to avoid the subjective one-sidedness of random sampling as much as possible, and the averages of each measured color region were also listed in Table 1. The results show that the contents of fluxing agents of Na_2O and CaO vary from 0.13 to 20.97 wt% and from 5.33 to 10.49 wt%, respectively. The distinct variations are thought to be attributed to the loss of fluxing agents caused by surface weathering of the ancient glass[8,28,32,33]. Therefore, it is reasonable to take the average chemical composition from three to eight measured points in each color region. It can be seen that the contents of Fe_2O_3, CuO, Sb_2O_3, CoO, and Mn_2O_3 in the four color regions are significantly different (see Table 1 and Fig. 6). Dark blue eye ball contains higher CoO (0.11 wt%) and Fe_2O_3 (2.23 wt%) without Mn_2O_3, while other color regions do not contain CoO [Fig. 6(b)]. It indicates that the raw material of the cobalt colorant probably contains high iron. The Co^{2+} ion makes glass with a translucent to transparent blue even if with a concentration of a few tenths of one percent[17]. In ancient China, the cobalt ion was also used in colorizing the blue glaze upon the tricolored glazed pottery of the Tang Dynasty and blue and white porcelain of the Yuan and Ming Dynasties. The ions of Fe and Mn, which can be considered as the chromophore responsible for the brown color[4], were found in

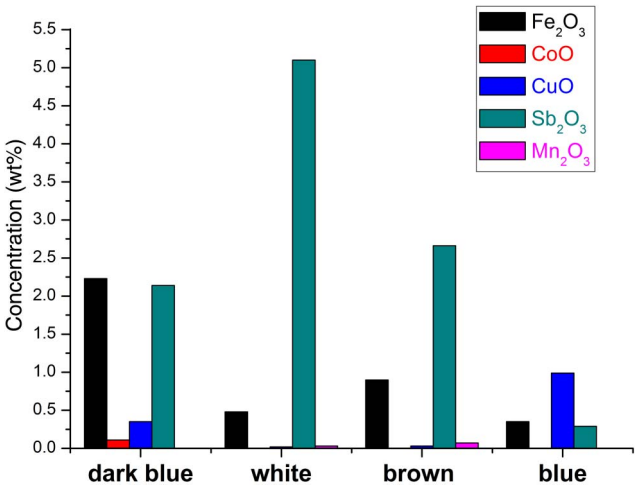

Fig. 6. Fe_2O_3, CuO, Sb_2O_3, CoO, and Mn_2O_3 contents in different color regions of eye bead HXX-M10.

the brown layers containing high concentrations of Fe_2O_3 (0.90 wt%) and Mn_2O_3 (0.07 wt%). The chemical results expressed as oxides consider all the iron as Fe^{3+}, but both Fe^{3+} and Fe^{2+} are glass colorants, and their ratio determines the glass color. According to previous research[34], the amber-brown color of ancient glass, which was melted under an oxidizing atmosphere, could be caused by the Fe^{3+} ions. The colorant CuO shows relatively high concentrations (from 0.72 to 1.20 wt%) in the turquoise blue matrix. In general, bivalent Cu^{2+} ions make the glass blue. Some addition of copper to the glass recipe turns the color of yellow beads to green[35]. A noticeable amount of Sb_2O_3 (5.10 wt%) and CaO (7.90 wt%) were detected in white layers. Additionally, a small amount of Sb_2O_3 in the turquoise blue matrix, brown, and dark blue regions was also detected. According to the results of OCT and micro-analysis above, we could infer that it is probably caused by the infiltration of Sb_2O_3 when the hot white frit was inlaid into the matrix.

To characterize the phases of the different color regions, confocal μ-RS was used for non-destructive analysis of the eye bead. The amorphous states were quite easily discriminated by the Si–O stretching (i.e., ~1000 cm^{-1}) and bending (~500 cm^{-1}) envelopes in the dark blue, turquoise blue, and brown white color regions [Fig. 7(a)]. It indicates that the matrix of the bead is of glassy material. However, crystal phases were also identified from the opacified white layers by μ-RS. Most of them are calcium antimonate (hexagonal $CaSb_2O_6$) with the characteristic Raman bands at around 234, 320, 332, and 668 cm^{-1} that are in good agreement with published values[22,36]. In ancient Egypt and other Eastern Mediterranean areas, $CaSb_2O_6$ was usually used as an opacifier/colorant in vitreous materials such as faience, frit, and glass to present opaque white[37]. Figure 7(c) shows that the hexagonal $CaSb_2O_6$ crystal was overlapping the Si–O bending envelope in the dark blue eye ball, which is consistent with the results of

μ-XRF analysis. Furthermore, the bands near 261, 329, 480, 507, 567, and 791 cm^{-1} [Fig. 7(d)], in accordance with oligoclase $[(Na, Ca)(Si, Al)_4O_8]$[38,39], a probable unfused raw material, were observed in the white eye region.

The non-destructive technique of OCT, supplemented with a digital microscope, provided a quick and easy view of the cross-section structure and uniformity. μ-XRF proved to be a highly effective method for non-destructive analysis of the multicolored glass eye beads unearthed in the Henan Province. Different color regions can be detected quickly through high-speed screening and can be visualized using image processing. However, the main limitation of μ-XRF is the impossibility of identifying the chemical compounds. This difficulty could be overcome using μ-RS. On the other hand, RS cannot detect colorants in glass if they are transition ions. The complementary use of different techniques is necessary for full identification of the information present in ancient glass. These data reveal that the eye bead is a stratified glass produced by hot-working, i.e., the turquoise blue matrix was firstly produced, and then the white layers, brown layers, and the dark blue eye ball were successively embedded into the matrix in a semi-solidified state. The ancient glass maker consciously chose different coloring materials to produce the multicolored glass beads. Dark blue, turquoise blue, and brown colors originate from ions of Co, Cu, and Fe and Mn, respectively. Beyond the transition metal ions, chemical compounds, for example, the hexagonal $CaSb_2O_6$, are a key factor in the white layers of the glass bead. It was used to produce an opaque white color, as a representative colorant and opacifier in the ancient Egypt and Eastern Mediterranean areas. We can conclude that the eye bead is typical western ancient natron-type soda-lime glass introduced to China through the Northern Silk Road from Egypt or the Eastern Mediterranean areas. It is a witness of the cultural and economic exchanges between China and foreign countries about 1400 years ago.

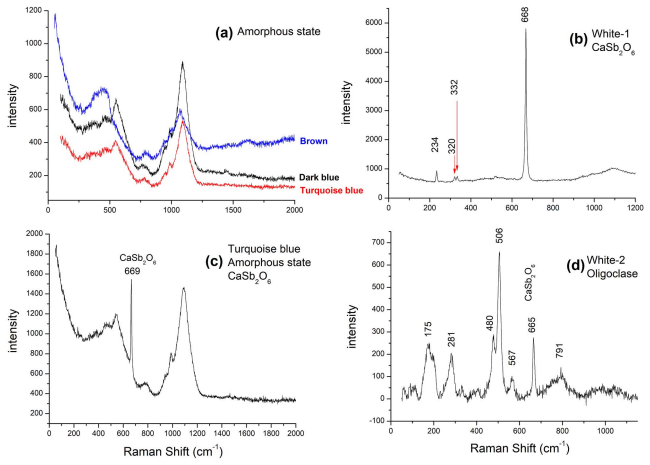

Fig. 7. Raman spectra of different color regions of eye bead HXX-M10. (a) Raman spectra of dark blue eye ball, turquoise blue matrix, and brown layer; (b) $CaSb_2O_6$ crystal in white circles; (c) envelope bands of turquoise blue matrix and $CaSb_2O_6$ crystal; (d) Oligoclase and $CaSb_2O_6$ crystals in a white layer. $\lambda = 532$ nm.

This Letter is devoted to exploring a new non-destructive combination of analytical techniques for the study of the cross-section structures, fluxing agents, colorants, and micro-phases of an archaeological multicolored stratified glass eye bead. This work demonstrates the possibility of deriving effectively and conveniently the information on glass-making technology, chemical systems, and provenance, using the different complementary techniques without any sampling or sample preparation in line with the recommended ethical guidelines for cultural heritage research. The combination could be widely used for researching cultural heritage such as porcelain, glazed pottery, faience, polychrome ceramic, wall painting, and jade artifacts.

This research was supported by the National Key R&D Program (No. 2019YFC1520203) and the National Social Science Foundation of China (NSSF) (No. 18AZD029). We also extend our thanks to Ms. Ting Xiao and Ms. Jing Shen of Horiba (China) Trading Co., Ltd. for their help in the μ-XRF experiment.

References

1. K. Egodage, C. Matthäus, S. Dochow, I. W. Schie, C. Härdtner, I. Hilgendorf, and J. Popp, Chin. Opt. Lett. **15**, 090008 (2017).
2. J. Q. Dong, Q. H. Li, and X. Yan, Chin. J. Nat. **5**, 325 (2015).
3. Y. M. Yang, L. H. Wang, S. Y. Wei, G. D. Song, J. M. Kenoyer, T. Q. Xiao, J. Zhu, and C. S. Wang, Microsc. Microanal. **19**, 335 (2013).
4. F. X. Gan, Q. H. Li, and J. Henderson, *Recent Advances in the Scientific Research on Ancient Glass and Glaze* (World Scientific, 2016).
5. Q. H. Li, J. C. Yang, L. Li, J. Q. Dong, H. X. Zhao, and S. Liu, Spectrochim. Acta A **138**, 609 (2015).
6. F. X. Gan, H. S. Cheng, Y. Q. Hu, B. Ma, and D. H. Gu, Sci. Chin. Technol. Sc. **52**, 922 (2009).
7. P. Colomban, Appl. Phys. A **79**, 167 (2004).
8. J. Q. Dong, Q. H. Li, and S. Liu, X-Ray Spectrom. **44**, 458 (2015).
9. C. Kharmyssov, M.W. L. Ko, and J. R. Kim, Chin. Opt. Lett. **17**, 011701 (2019).
10. L. D. Zhu, Y. Wang, Y. Yuan, H. X. Zhou, Y. Q. Zhao, and Z. H. Ma, Chin. Opt. Lett. **17**, 041701(2019).
11. Y. Huang, C. C. Wu, S. Y. Xia, L. Liu, S. L. Chen, D. D. Tong, D. N. Ai, J. Yang, and Y. T. Wang, Chin. Opt. Lett. **17**, 051001 (2019).
12. A. G. Attaelmanan, X-Ray Spectrom. **43**, 325 (2015).
13. D. X. Zhong, M. S. Guo, Y. Q. Hu, S. Liu, J. Q. Dong, and Q. H. Li, Spectrosc. Spect. Anal. **39**, 178 (2019).
14. X. Yan, J. Q. Dong, Q. H. Li, M. S. Guo, and Y. Q. Hu, Chin. J. Lasers **41**, 0908001 (2014).
15. H. Aoyama, K. Yamagiwa, S. Fujimoto, J. Izumi, R. Ishikawa, S. Kameshima, and T. Arakaki, X-Ray Spectrom. **47**, 265 (2018).
16. K. Yamagiwa, S. Fujimoto, H. Aoyama, J. Izumi, S. Kameshima, and T. Arakaki, J. Archaeol. Sci. Rep. **26**, 101879 (2019).
17. M. L. Franquelo, A. Duran, J. Castaing, A. A. David, and J. L. Pérez-Rodríguez, Talanta. **89**, 462 (2012).
18. E. Arizio, E. F. Orsega, R. Falcone, and M. Vallotto, Environ. Sci. Pollut. Res. Int. **21**, 13243 (2014).
19. P. Colomban, J. Non-Cryst. Solids. **323**, 180 (2003).

20. P. Colomban, T. Aurélie, and L. Bellot-Gurlet, J. Raman Spectrosc. **37**, 841 (2006).
21. A. Tournié, L. C. Prinsloo, and P. Colomban, J. Raman Spectrosc. **532**, 43 (2011).
22. H. C. Beck, Archaeologia **77**, 1 (1928).
23. S. M. Kwan, *Early Chinese Glass* (Chinese University of Hong Kong, 2001).
24. Q. H. Li, S. Liu, H. X. Zhao, F. X. Gan, and P. Zhang, Archaeometry **56**, 601 (2014).
25. H. X. Zhao, Q. H. Li, S. Liu, and F. X. Gan, J. Raman Spectrosc. **44**, 643 (2013).
26. Q. H. Li and J. Q. Dong, Natl. Pal. Mus. Mon. Chin. Art **421**, 42 (2018).
27. D. Y. Zhao, Acta Arch. Sin. **2**, 177 (2012).
28. S. Liu, F. X. Gan, and Q. H. Li, Spectrosc. Lett. **48**, 302 (2015).
29. H. X. Zhao and Q. H. Li, J. Raman Spectrosc. **48**, 1103 (2017).
30. A. Bonneau, J. F. Moreau, R. G. Hancock, and K. Karklins, Beads **26**, 35 (2014).
31. J. Q. Dong, Q. H. Li, and S. Liu, X-Ray Spectrom. (2020).
32. S. Liu, Q. H. Li, Q. Fu, F. X. Gan, and Z. M. Xiong, X-Ray Spectrom. **42**, 470 (2013).
33. S. Liu, Q. H. Li, F. X. Gan, and J. Lankton, J. Archaeol. Sci. **39**, 2128 (2012).
34. M. García-Heras, J. M. Rincón, A. Jimeno, and M. A. Villegas, J. Archaeol. Sci. **32**, 727 (2005).
35. K. H. Wedepohl, *Glas in Antike und Mittelalter: Geschichte eines Werkstoffs* (Schweizerbart, 2003).
36. E. Husson, Y. Repelin, and M. T. Vandenborre, Spectrochim. Acta A **40**, 1017 (1984).
37. M. S. Tite and A. J. Shortland, *Production Technology of Family and Related Early Vital Materials* (University of Oxford, 2008).
38. J. Xie, "A Raman spectroscopy study of hyperfine structure of aluminosilicate and feldspar," Master's Thesis (China University of Geosciences, 2008).
39. T. P. Mernagh, J. Raman Spectrosc. **22**, 453 (1991).